Traffic & Transportation

Enhanced Social Force Model for Microscopic Traffic Flow Simulation in Mixed Traffic Scenarios

Yuzhu YANG[1], Dan ZHOU[2], Zhilong WU[3]

Original Scientific Paper
Submitted: 15 Jan 2025
Accepted: 7 July 2025
Published: 30 Mar 2026

[1] 2197326926@qq.com, School of Architecture and Transportation Engineering, Guilin University of Electronic Technology, Guilin, China
[2] Corresponding author, 8697992@qq.com, School of Architecture and Transportation Engineering, Guilin University of Electronic Technology, Guilin, China
[3] 791105165@qq.com, School of Architecture and Transportation Engineering, Guilin University of Electronic Technology, Guilin, China

Publisher:
Faculty of Transport and Traffic Sciences, University of Zagreb

ABSTRACT
With the widespread adoption of e-bikes, mixing with cars is becoming increasingly common, which raises concerns about traffic safety and efficiency. In this paper, we improve the social force model based on the artificial potential energy field and construct a microscopic simulation platform with the machine-non-mixed road section as the research object. Using high-precision trajectory data, we analyse the characteristics of machine-non-mixed flow, propose a shield-shaped perception domain to adapt to the actual driving perception, and construct boundary force and lane force to compensate for the deficiencies of traditional models. After completing the calibration of the model parameters, a micro-simulation platform compatible with various functions is constructed to verify the validity of the model and analyse the capacity and overtaking situation under different lane widths and vehicle ratios, thus providing a theoretical basis for the design of road segregation facilities and traffic management.

KEYWORDS
mixed traffic; social force model; microscopic traffic flow; artificial potential field; simulation verification.

1. INTRODUCTION

With the advantages of convenience, economy and labour-saving, electric bicycles have become the primary choice for urban residents' short-distance travel, with an average annual sales volume exceeding 35 million units and a social retention rate of 350 million units. Although the new national standard will raise the speed limit to 25 km/h, the actual riding speed is still generally exceeded, the average speed is 40% to 50% higher than that of the traditional bicycle, and the related traffic accident rate is 8.9 times higher than that of the traditional bicycle, highlighting the high expectation of speed and potential risks. In the old urban areas of small and medium-sized cities, the non-motorised lanes are often softly segregated by demarcation on secondary roads, side streets and other narrow road sections, but the swerving and overtaking of non-motorised vehicles and the temporary occupation of motorised vehicles leads to an intensification of the conflict between mixed traffic, which seriously affects the efficiency of traffic flow and safety. In this context, a key challenge is to optimise road design and improve road safety by analysing the micro-interaction mechanism of mixed traffic flow and constructing high-precision simulation models.

Researchers at home and abroad have analysed the characteristics of mixed traffic from three perspectives: speed-density relationship, safety distance and behavioural heterogeneity. In general mixed traffic research, non-motorised vehicles are usually considered as interference factors for motorised vehicles. Zhanguo et al. [1] investigated the speed changes of motorised vehicles under three types of bicycle interference and analysed the effects of non-motorised lane service level and bicycle flow density. Guibao et al. [2] pointed out that as

the density of bicycles increases, some bicycles will enter the motor vehicle lane, causing the motor vehicle operating speed to decrease significantly, and the number of motor vehicle lanes and the width of bicycle lanes have a significant impact on motor vehicle operation. Xue et al. [3] found that at low to medium densities, lateral oscillations exacerbate the mutual interference between motorised and non-motorised traffic, increase the number of bicycle crossings, and reduce the efficiency of motorised vehicles, and that mixed traffic generates more crossings than homogeneous bicycle traffic. Lihui et al. [4] quantified the effect of the number of roadside bicycles on motor vehicle operations on arterial roads from a capacity perspective and found that an increase in the number of roadside bicycles increases the saturated headway and significantly reduces the average speed and capacity of motor vehicles in the adjacent lanes. Schaefer et al. [5] demonstrated that on a low-capacity urban road with no non-motorised lanes, motor vehicle speeds are generally not reduced by more than 1 mph after bicycle interference. Apasnore et al. [6] analysed the factors affecting the lateral distance between bicycles and cars and their impact on driver comfort and found that vehicle speed, ambient traffic density, number of lanes and lane width significantly affect overtaking distance and driver comfort. Dailisan et al. [7] used motorcycles and cars to determine the critical values at which the interactions of lane changing and random and non-random deceleration strongly influence vehicle speed. Shao et al. [8] examined vehicle speeds before and after illegal lane-changing behaviour based on a non-cooperative strategy model with perfect information, and analysed and quantified the risk of lane-changing behaviour in terms of the risk level per unit number of road conflicts. Liu et al. [9] used the critical lateral distance as an indicator of the strength of the interaction and modelled the lateral interaction using the acceleration failure time (AFT) model with a Weibull distribution parameter. Petzoldt et al. [10] found that as the speed of an e-bike increases, its distance from motor vehicles decreases, and the distance between an e-bike and a motor vehicle is smaller than that of a conventional human-powered bicycle.

Four types of models have been used to characterise mixed traffic flows:

(1) Follower models: Tang et al. [11] proposed three individual friction-based follower models for non-uniform traffic flows consisting of cars, bicycles and pedestrians, and the results showed that bicycle and pedestrian densities exacerbate friction effects, thus reducing speeds and throughputs. Mathew et al. [12] proposed a spatially discretised mixed-flow follower model that simulates longitudinal and lateral movements of vehicles by dividing a lane into multiple strips, allowing vehicles to overtake across the strips. Papathanasopoulou et al. [13] proposed a data-driven mixed-flow modelling approach, which combines virtual lane width estimation to simplify the modelling process and improve the reliability of the model.

The model is simple and easy to understand, but has limitations in mixed-flow applications: on the one hand, it is difficult to accurately adjust the width to simulate continuous longitudinal and lateral movements when dividing virtual lanes or sub-lanes; on the other hand, the model cannot adequately reflect the physiological and psychological influences of motorised and non-motorised drivers, and has weak interpretations of complex traffic behaviours in a mixed flow.

(2) Cellular automata (CA) model: Meng et al. [14] analysed the lane-changing behaviour of motorcycles and proposed a single-lane cellular automata model for mixed traffic flow of cars and motorcycles. Jia Ning et al. [15] used the EBCA1 model with stochastic deceleration to model the non-motorised flow for the flexibility of the bicycle flow and formed a multi-lane model with the motorised flow based on the NS model. Luo et al. [16] proposed that the constant occupancy rule may lead to the overestimation of the car flow in heterogeneous traffic flows, especially under different bicycle densities.

Due to its low computational complexity and ease of implementation, the NS model has been widely used in the field of unmixed traffic flow simulation, and research focuses on optimising and improving the established rules for specific scenarios. However, the model has the following problems in the study of machine-non-mixed traffic flow:

1) It cannot consider the influence of boundary conditions, such as lane lines and curbs, on individual vehicle cells, which should be considered important traffic facilities to limit and guide the trajectory of the mixed flow.
2) As a discrete model, the choice of parameters, such as step size and cell size, affects the motion state of individual cells only in the finite set of variations, and the manually set rules differ from the real scene, making it difficult to describe the crossing and overtaking behaviour of non-motorised vehicles in the mixed-flow section in a realistic and detailed way, and thus there is a major limitation in simulating the continuous interactions of mixed-flow vehicles.

(3) Social forces model: The classical social force model of Helbing [17] has been gradually applied to non-motorised vehicle studies after making a breakthrough in pedestrian flow studies. Zhang Rui et al. [18] took the vehicle being overtaken by proximity as the research object, improved the repulsion force and driving force between vehicles, and established an improved social force model to simulate the lateral offset and longitudinal deceleration and yielding behaviour of the overtaken vehicle. Rui et al. [19] proposed an improved social force model to describe the parallel and following behaviour of NMV flow. Qin et al. [20] introduced new behavioural forces to simulate the free movement, following and overtaking behaviour of NMV cyclists. Heying [21] analysed the mechanism of the median of a two-way cycle lane with opposite neighbours, improved the overtaking force, and constructed a microscopic simulation model for one-way cycling. Zixuan [22] constructed a social force model for left-turning non-motorised vehicles at intersections, which reproduced the left-turning non-motorised vehicle expansion phenomenon by boundary correction coefficients, and introduced the trajectory line boundary force to describe the driving characteristics of following the trajectory line. Weili et al. [23] extracted the trajectory data of e-bikes, used the horizontal and longitudinal distance and speed difference as the characteristic variables, established the decision rules of e-bikes, and proposed an improved social force model for one-way e-bike traffic.

The current microscopic models of mixed traffic flow are mainly based on bicycles and cars, but the study of the microscopic behaviour of e-bikes, as an economical and convenient means of transport, in the scenario of their mixing with cars has also received attention. Da et al. [24] introduced gap force, following force and repulsion force based on the traditional social force model to establish a heterogeneous traffic flow model applicable to the scenario of e-bike intrusion into motor vehicle lanes, and analysed the effects of e-bike queuing number and arrival rate on motor vehicle flow rate and passing speed. Qu et al. [25] proposed a microscopic traffic flow model for unmixed flow by analysing the interaction, lane-changing behaviour, and conflict between e-bikes and cars.

(4) Artificial potential field model: Jensen et al. [26] demonstrated that an artificial potential field model could naturally describe the driver's situational awareness and control their basic behaviours. Xu [27] proposed a two-dimensional model to simulate the turning behaviour of a mixed-flow intersection, where the planning layer uses the distance potential field to plan the ideal path, and the action layer realises the vehicle movement under the action layer of the artificial potential field. Xie [28] introduced the velocity and acceleration differential potential fields to ensure safe overtaking in dynamic environments. Zhang [29] constructs the bend gravitational potential field and the bend repulsive potential field based on a variety of functions, which constitute the search space for the overtaking path of a car in a bend.

In the study of the influence area of the repulsive potential field, some scholars [30-34] introduced the safety ellipse theory and used the elliptical distance to replace the actual distance in the traditional repulsive potential field. Wang et al. [35] reconstructed the area of the obstacle repulsive field according to the obstacle avoidance safety model to improve the artificial potential field method, and the adapted potential field can ensure that the vehicle maintains a certain degree of stability and safety when it performs the operations of obstacle avoidance and overtaking, and so on.

In the study of the road potential field, Kong Huifang et al. [36] introduced the road potential field function to describe the road boundary and solved the local optimisation problem by setting virtual target points. Wang Qidong et al. [37] constructed the road potential field function by considering two variable parameters, namely longitudinal speed and lateral speed, and solved the desired steering angle by the potential field gradient. Li Shengqin et al. [38] increase the road boundary repulsive potential field to ensure that the vehicle keeps a straight line after collision avoidance and introduce the speed adjustment factor to establish the dynamic obstacle potential field to solve the collision avoidance path planning problem under the dynamic obstacle. Hongyu et al. [39] propose an improved artificial potential field method considering the vehicle speed and incorporating the structure of the highway and traffic rules into the construction of the potential field of the road and traffic lanes.

Studies have shown that macroscopic models are difficult to characterise the behaviour of heterogeneous individuals, follow-the-leader models are difficult to analyse the complex decision-making processes such as lane changing and overtaking, meta cellular automata models are insufficient to characterise the role of continuity of physical boundaries on roads, and traditional social force models have a large deviation of vehicle trajectory prediction from the real environment due to the assumption of rigid yield avoidance. In this study, a new social force framework integrating the artificial potential field theory is proposed to unify the flexible guiding role of physical boundaries such as lane separation lines and curbs and the dynamic game behaviour between vehicles into one mechanical system by establishing a continuous gradient potential field, breaking

the limitation of the traditional model that the lane force is separated from the vehicle force. Compared to the improved strategy of superimposing the overtaking force, the framework makes the overtaking behaviour physically interpretable through the adaptive adjustment of the potential energy field strength and direction, while retaining the advantage of the social force model in characterising the individual differences of heterogeneous traffic flows, providing a more refined theoretical tool for traffic conflict prediction and path optimisation under the scenarios of non-mixed traffic.

This study focuses on the micro-interaction mechanism in the mixed traffic area of urban roads, and constructs an analysis framework in three stages:

1) Based on high-precision trajectory data, we analyse the characteristics of mixed traffic, extract the core parameters such as speed and density, and reveal the arrival pattern of non-motorised vehicles and the disturbance pattern of motorised vehicle flow by crossing the line;
2) Innovatively propose a social force improvement model integrating artificial potential field, reconstruct the dynamic perception domain of heterogeneous traffic flow (elliptical axial adjustable) by dividing the machine-machine, machine-non-machine and non-non-machine three-layer force system, and establish a coupling mechanism between the lane line potential field and the inter-vehicle potential field, thereby breaking through the shortcomings of the rigidity of the boundary constraints of the traditional model and the weakness of the explanatory nature of the crossing behaviour;
3) Developing a Python simulation platform, integrating the A* algorithm and the social force module, realising the visualisation and parameter calibration of the mixed traffic scene, and verifying the effectiveness of the model in predicting overtaking capacity and quantifying conflict risk. The study improves the micro-behavioural modelling system of heterogeneous traffic flow at the theoretical level and provides digital decision-making tools for urban road space optimisation and non-motorised vehicle control at the application level.

2. ANALYSIS OF TRAFFIC FLOW CHARACTERISTICS ON NON-MIXED ROAD SECTIONS WITH ONE MACHINE

In this paper, video vehicle trajectory data are extracted based on the field aerial photography data in the non-motorised area, combined with the research results of the subject team [40]. Aiming to address the problem of small size and low detection accuracy of non-motorised vehicles, the trajectory data extraction method, which consists of four parts: UAV video stabilisation, vehicle detection, vehicle tracking and spatial coordinate mapping, is improved. First, the UAV aerial video is stabilised using the optical flow method to eliminate the image jitter caused by engine operation and external wind. Then, the enhanced YOLOx vehicle detection algorithm is used to obtain the vehicle bounding box. For the occlusion problem, the Deep Sort algorithm is used for high-precision vehicle tracking. Finally, the initial trajectory data under the pixel coordinate system are converted to real physical coordinates to form continuous actual road vehicle trajectory data.

Based on the data obtained by the research group, the behavioural characteristics of individuals involved in microscopic traffic flow can be roughly divided into transverse and longitudinal characteristics, serpentine trajectories, parallelism and overtaking, etc., and the contents of the investigation and analysis in this subsection can provide a basis for the establishment of the research model as well as the simulation validation.

2.1 Vehicle inspection

At present, deep learning target detection algorithms are mainly divided into two-stage detection methods (two-stage) and one-stage detection methods (one-stage). One-stage detection method does not need a region candidate network (RPN), and directly regresses the target category probability and position coordinates, with an obvious speed advantage. Among them, the YOLO series algorithms have developed rapidly due to their versatility, fast detection speed and low background misdetection. In 2021, the YOLOx algorithm introduced by Kuangxue Technology [41] further improved the detection accuracy and speed through improvements such as dynamic sample matching, decoupling of the detection head and the FOCUS module, which is suitable for end-to-end deployment. In this paper, the YOLOx algorithm for vehicle detection is used and improved to enhance the detection accuracy for small targets. The improvement points include the median pooling-based convolutional block attention module (M-CBAM), which enhances the learning ability of target edge and texture features by adding a median pooling layer in the channel and spatial attention module, and at the same time reduces the model parameters to reduce the computational cost, and the addition of a fourth small target detection head, which improves the model's small target detection performance and compensates for the small

target features that may be lost in the feature extraction process. The YOLOx algorithmic network structure is shown in *Figure 1*, which is mainly divided into Darknet, which combines cross-stage localised networks, space pyramid pooling bottleneck layer and the YOLO decoupling head.

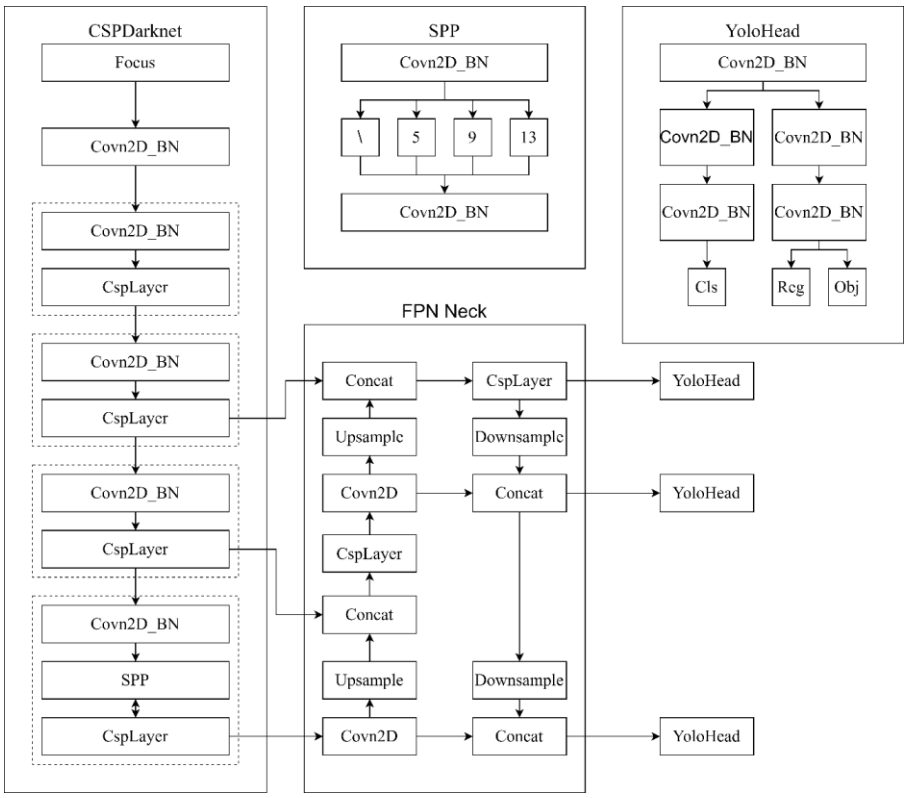

Figure 1 – YOLOx algorithmic network structure

2.2 Vehicle tracking

Target tracking is an important research direction in computer vision, and with the development of target detection technology, it is widely used in the field of transportation. In this paper, for the occlusion problem caused by factors such as greenery and traffic lights on urban roads, the Deep Sort multi-target tracking algorithm is used to obtain the trajectory information of moving vehicles. Deep Sort was proposed by Wojke et al. [42] in 2017 and is improved based on the Sort algorithm proposed by Bewley et al. [43] in 2016. The Sort algorithm has a high tracking speed and accuracy, but it is less effective when the target is occluded. Deep Sort introduces target appearance information to reduce the number of ID exchanges during occlusion and improve tracking performance. The main process includes: the prediction phase, Kalman filtering to predict the target tracking frame in the next frame; the matching phase, data association through cascade matching and IOU matching; the update phase, Kalman filtering to update the results and reduce the error.

2.3 Data preprocessing

After mapping the extracted trajectory data to the real physical coordinates, the speed and acceleration of the vehicle can be obtained by using the five-point differential equation with first-order derivatives and the five-point differential equation with second-order derivatives, with the formulae shown in *Equations (1)* and *(2)*, respectively. By measuring the angle between the vehicle line and the set auxiliary line in the trajectory data, the angular indexes of the vehicle, such as the heading angle and the turning angle, can be derived.

$$velocity = \frac{f(t-2h) - 8f(t-h) + 8f(t+h) - f(t+2h)}{12h} \tag{1}$$

$$acceleration = \frac{-f(t-2h) + 16f(t-h) - 30f(t) + 16f(t+h) - f(t+2h)}{12h^2} \tag{2}$$

In the formulas: t is the current time; h is the time interval.

2.4 Analysis of horizontal and vertical characteristics

From *Figure 2*, it can be seen that when the non-motorised vehicle is travelling, the driver is aware of keeping a safe distance, and there is a certain psychoactive safety distance. In terms of horizontal distribution, the horizontal distance between the vehicle in front and the vehicle is basically greater than 1.5 m, and the distance can reach a greater distance if the traffic conditions allow; and when the non-motorised vehicle is travelling at a low speed or waiting for a traffic light, the psychoactive safety distance will be reduced accordingly. In terms of longitudinal characteristics, the following distance between the vehicle and the vehicle in front is relatively close, about 1 m, and this close safety distance is maintained even at low speeds. At the same time, the cyclist will actively maintain a larger safety distance from the non-motorised vehicle behind. In addition, the radar map shows that the number and density of approaching vehicles are different between the front and rear of the vehicle, which is due to the principle of screening the nearest vehicles in the direction of travel of the vehicle. Once the vehicle stops, the number and density of approaching vehicles in front and behind the vehicle converge to the same number and density.

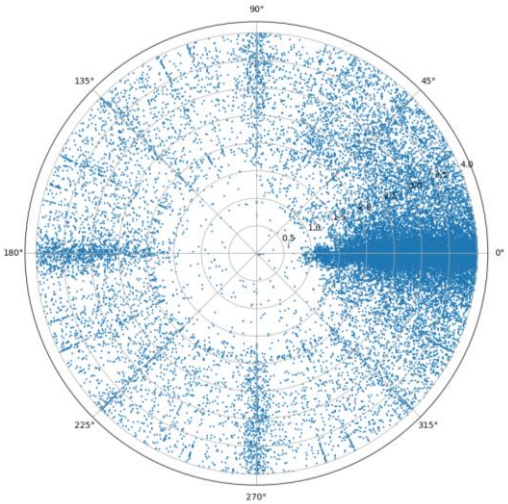

Figure 2 – Radar map of vehicle distribution around non-motorised vehicles (Distance between each floor 0.5 m)

2.5 Serpentine trajectory

Non-motorised vehicles, especially two-wheeled electric vehicles, tend to exhibit a wobbling trajectory due to their poor stability during travel, a phenomenon referred to as the objective trajectory width [44]. Unlike bicycles that require pedalling, electric two-wheelers are primarily powered by electricity, so their trajectory width is more closely related to the riding speed rather than the rider's physical strength. Based on the research by Li [45] and research data (as shown in *Figure 3*), when the speed of an electric two-wheeler is 7 km/h or less, the meandering trajectory width averages 29 cm, and when the speed exceeds 7 km/h, the trajectory width significantly increases to 36 cm. The average meandering trajectory width for two-wheeled electric vehicles is 34 cm, a measurement that can also be influenced by riding habits and vehicle models.

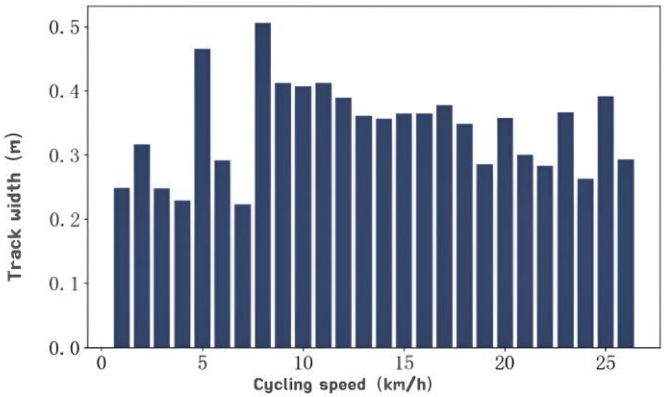

Figure 3 – Non-motorised objective trajectory width statistics

2.6 Parallel and beyond situations

In overtaking manoeuvres, non-motorised vehicles often take the lead due to road conditions and their agility, whereas motorised vehicles, being less numerous, overtake non-motorised vehicles relatively less frequently. Right-turning motor vehicles overtake non-motorised vehicles more frequently because traffic signals do not restrict them, while non-motorised vehicles travelling straight often slow down or stop due to traffic lights. Due to the design of single lanes and limitations in numbers, overtaking behaviours among motor vehicles are relatively infrequent. Investigating the number and type of vehicle parallels and overtaking between carpools in the data, our team tallied the data as shown in *Figures 4, 5* and *6.*

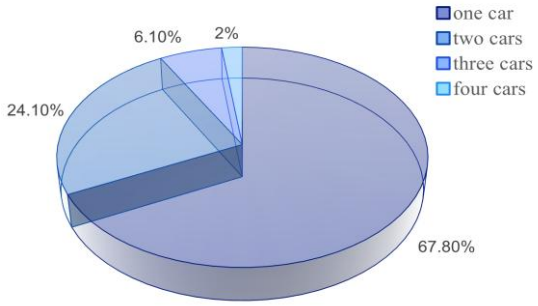

Figure 4 – Statistical chart of the number of vehicles in parallel

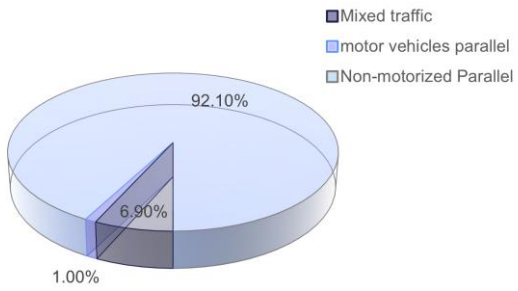

Figure 5 – Vehicle parallel type statistical chart

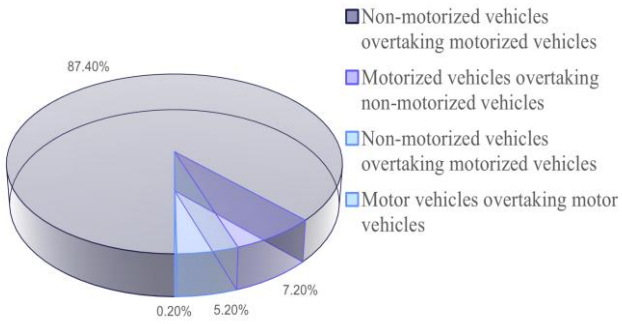

Figure 6 – Vehicle override type statistics

3. A MICRO TRAFFIC FLOW MODEL FOR MIXED TRAFFIC AREAS OF MOTOR VEHICLES AND NONMOTOR VEHICLES BASED ON AN IMPROVED SOCIAL FORCE MODEL

Existing research and practice have proven that road elements are crucial for traffic safety [46]. This study focuses on urban old-town areas where motorised and non-motorised vehicles share the road on secondary roads, branch roads and auxiliary lanes. Due to limited space, these sections can only be softly separated by designating a dividing line between motorised and non-motorised traffic. The research assumptions include the absence of hard isolation facilities, the composition of one motor vehicle lane and one non-motor vehicle lane, being located far from the entrances and exits of residential areas and parking lots, having smooth road surfaces, all non-motorised vehicles being two-wheeled electric vehicles, and the exclusion of pedestrians and other traffic participants. The study period is during morning and evening rush hours, excluding the influence of extreme weather and insufficient lighting. The mixed machine/non-mixed traffic flow scenario is shown in *Figure 7.*

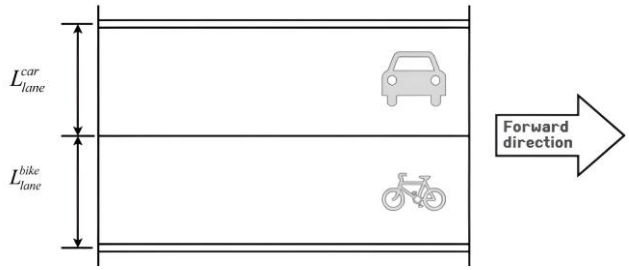

Figure 7 – Road traffic environment

3.1 Design of the non-motorised vehicle perception domain

Formula design for non-motorised vehicle perception domain range

During the driving process, to avoid conflicts or collisions with other traffic participants and to maintain a certain level of driving comfort, drivers will keep a certain psychological safety space. It is generally believed that other individual units entering this space will have a strong influence on the driver [47-50]. Therefore, this area of influence is referred to as the "perception field".

Given that the centre point of an ellipse is (0,0), the semi-major axis length is a, and the semi-minor axis length is b, its parameter equation on the spatial Cartesian coordinate system XOY is:

$$\begin{cases} x = a\cos(\theta), \theta \in [0,2\pi] \\ y = b\sin(\theta), \theta \in [0,2\pi] \end{cases} \tag{3}$$

(1) Design of the limited perception effect formula:

In the spatial construction of the cyclist's perception field, since more information is perceived from the front and less from the back, this paper introduces an anisotropy coefficient λ_i^s to describe the phenomenon of uneven distribution of the perception field in space. The schematic diagram of the non-motorised vehicle perception domain is shown in *Figure 8.*

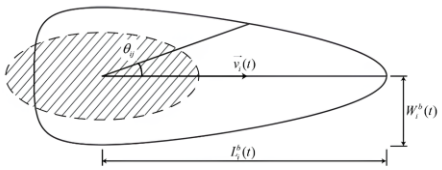

Figure 8 – Schematic of the non-motorised sensory domain

Let the limited perceptual effect be LPE(θ): For limited perceptual effects, the geometric expression in a given coordinate system is: LPE(0)=LPEmax and LPE(π)=LPEmin. Assuming the perceived effect value in the vertical positive direction is 1 and the perceived effect value in the vertical negative direction is the anisotropy coefficient λ^s, the following equation can be established:

$$LPE(\theta) = \lambda^s + (1-\lambda^s)\frac{1+cos\,\theta}{2} \tag{4}$$

Equation (2) satisfies LPE(0)=1 and LPE(π)= λ^s. Furthermore, for the function described by *Equation (2)*, as the value of θ approaches π from both ends, two abrupt peaks occur, a phenomenon that is particularly noticeable when λ^s is close to 0. To address this, an anisotropy adjustment factor s_λ, which is greater than 1, is incorporated. This adjustment factor helps to smooth out the transitions in the function's behaviour, reducing the abruptness of the peaks and providing a more gradual change in the perception field as θ approaches π:

$$LPE\theta=\lambda s+1-\lambda s1+cos\theta 2s\lambda \tag{5}$$

At this point, the perceived effect value in the vertical positive direction is still 1, and the perceived effect value in the vertical negative direction becomes $(\lambda^s)^{s_\lambda}$.

(2) Design of dynamic compression effect formula:

Cyclists' perception of their surrounding traffic is limited by their perceptual capabilities and riding characteristics, which is manifested as an inverse relationship between the perception range of non-motorised vehicles and traffic flow density: at low density, there is faster vehicle speed and wider spacing; at high density,

there is slower vehicle speed and narrower spacing. This phenomenon is referred to as the dynamic compression characteristic. To precisely describe this characteristic, this paper introduces a compression effect value β, and based on the fundamental diagram characteristics established in traffic flow operation as referenced in [51], a dynamic compression effect expression *(Equation (6))* is formulated:

$$\beta=kjk \tag{6}$$

In the formula: k_j is the blocking density; k is the current traffic density.

Thus, it can be understood that the longitudinal effect value η^h is composed of two parts: first, half of the length of the major axis a_{bic} of the elliptical physical model of the non-motorised vehicle; and second, the safety distance necessary for the cyclist to react to the road conditions ahead. This distance is directly proportional to the product of the dynamic compression effect value β established by *Equation* (7)*,* the longitudinal reaction coefficient α^h and the velocity of the vehicle at time t, denoted as $\vec{v}(t)$:

$$\eta h=12abic+\alpha h\beta\|vt\| \tag{7}$$

(3) Horizontal appearance formula design:

The established lateral perception field (VPF) of non-motorised vehicles is composed of two parts: first, half of the length of the minor b_{bic} of the elliptical physical model of the non-motorised vehicle; and second, the lateral safety distance d^{vb} of the non-motorised vehicle. The following equation can be established to represent this:

$$VPF=\frac{1}{2}b_{bic}+d^{vb} \tag{8}$$

(4) Design of non-motorised vehicle perception domain range formula:

Based on *Equations (3), (5), (7)* and *(8),* one can derive the formula for the perception field range of non-motorised vehicles. For *Equation (2)*, the expressions for the variables a and b are as follows:

$$\begin{aligned} a &= \eta^h LPE(\theta)=\left(\frac{1}{2}a_{bic}+\alpha^h\beta\parallel\vec{v}(t)\parallel\right)\left[\lambda^s+(1-\lambda^s)\frac{1+cos\,\theta}{2}\right]^{s_\lambda} \\ b &= VPF=\frac{1}{2}b_{bic}+d^{vb} \end{aligned} \tag{9}$$

Assuming that $L_i^b(t)$ and $W_i^b(t)$ are the longitudinal and transverse perception domain radii of non-motorised vehicles, the parameter equation of the perception domain of non-motorised vehicles on the spatial Cartesian coordinate system XOY is:

$$\begin{cases} L^b(t)=\left(\frac{1}{2}a_{bic}+\alpha^h\beta\parallel\vec{v}(t)\parallel\right)[\lambda^s+(1-\lambda^s)\frac{1+cos\,\theta}{2}]^{s_\lambda}\cdot cos\,\theta \\ W^b(t)=(\frac{1}{2}b_{bic}+d^{vb})\cdot sin\ \theta \end{cases} \tag{10}$$

Geometric description of non-motorised vehicle perception domain range

The perceptual model formula, after introducing individual units i and j into *Equation (10)* for symbolic representation, is shown in *Equation (11):*

$$\begin{cases} L_i^b(t)=\left(\frac{1}{2}a_{bic}+\alpha_i^h\beta\parallel\vec{v_i}(t)\parallel\right)[\lambda_i^s+(1-\lambda_i^s)\frac{1+cos\,\theta_{ij}}{2}]^{s_\lambda}\cdot cos\ \theta_{ij} \\ W_i^b(t)=(\frac{1}{2}b_{bic}+d^{vb})\cdot sin\ \theta_{ij} \end{cases} \tag{11}$$

In the formula: $L_i^b(t)$ and $W_i^b(t)$ are the longitudinal and transverse perception domain radii of non-motorised vehicles, respectively. a_{bic} and b_{bic} are the longitudinal and transverse axis lengths of the ellipse in the physical model of a non-motorised vehicle. α_i^h is the longitudinal response coefficient; β is the compression effect value; $\vec{v_i}(t)$ is the speed of the vehicle at time t; λ_i^s is the anisotropy coefficient; θ_{ij} is the angle between the actual velocity direction of the individual unit I and the line connecting the normal vectors of individual unit i and j. s_λ is the anisotropic adjustment coefficient and d^{vb} is the lateral safety distance for non-motorised vehicles.

3.2 Construction of individual units for non-mixed flows

The physical model established in this paper is based on traditional traffic flow and does not take into account intelligent connected and autonomous vehicles. A driver must operate the vehicle to complete transportation tasks. Therefore, when modelling, the vehicle and the driver are considered as a single entity for research purposes.

Physical modelling of motor vehicles and nonmotor vehicles

Based on the characteristics of motorised and non-motorised vehicles obtained from the investigation and analysis, the physical modelling can be referred to in *Figures 9* and *10*:

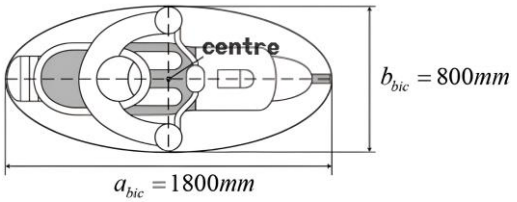

Figure 9 – Schematic diagram of a non-motorised individual unit

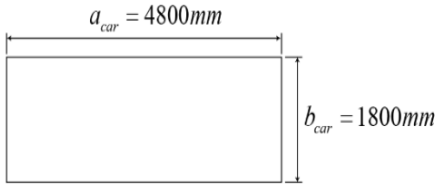

Figure 10 – Schematic diagram of motor vehicle unit

Perception domain range of motor vehicles

In this paper, the perception model for individual motor vehicles is shown in *Equation (12)*:

$$\begin{cases} L_i^c(t) = a_{car} + 2d_i^{hc} \\ W_i^c(t) = b_{car} + 2d_i^{vc} \end{cases} \tag{12}$$

In the formula: $L_i^c(t)$ and $W_i^c(t)$ are the longitudinal and transverse distances in the perception domain of motor vehicles, respectively. a_{car} and b_{car} are the longitudinal and transverse lengths of the rectangle of the physical model of the motor vehicle, respectively. d_i^{hc} and d_i^{vc} are the longitudinal and transverse perception distances of the motor vehicle, respectively. The schematic diagram of the motor vehicle perception domain is shown in *Figure 11.*

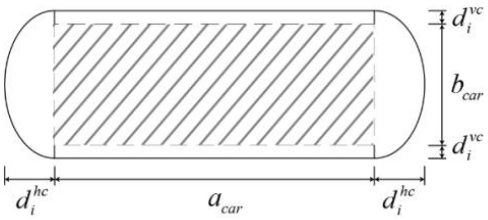

Figure 11 – Schematic diagram of the motor vehicle perception domain

3.3 Micromechanical model of mixed flow between motor vehicles and nonmotor vehicles

The social force model examined in this paper principally focuses on the driving force, inter-individual interaction force (comprising attraction and repulsion), and lane force and boundary force, which have been enhanced based on the artificial potential field model. The resultant force is ultimately calculated to establish the improved social force model.

Driving force

In the absence of external forces, drivers tend to travel at their desired speed, but this is often constrained by traffic and environmental factors. The subjective intention of an individual unit to adjust direction and speed to approach an ideal state is translated into a driving force, with the strength of the force increasing as the difference from the ideal state becomes greater. Under normal circumstances, the current speed of an individual unit will not exceed its desired speed, and this section of the analysis does not consider the special case where the speed exceeds the desired speed. The driving force in this paper is derived from the traditional social force model formula [39], and the expression for the driving force of the i-th vehicle at time t is shown in *Equation (13)*:

$$\vec{f_i^{dr}} = m_i \frac{v_i^0(t)\vec{e}_i^0(t) - \vec{v}_i(t)}{\tau_i} \tag{13}$$

In the formula: m_i is the vehicle mass, $v_i^0(t)$ is the expected speed of the vehicle ;$\vec{e}_i^0(t)$ is the expected direction of motion, parallel to the direction of the road's advanced $\vec{v}_i(t)$ of the vehicle at time t; τ_i is the duration. The schematic diagram of the driving force on individual units is shown in *Figure 12.*

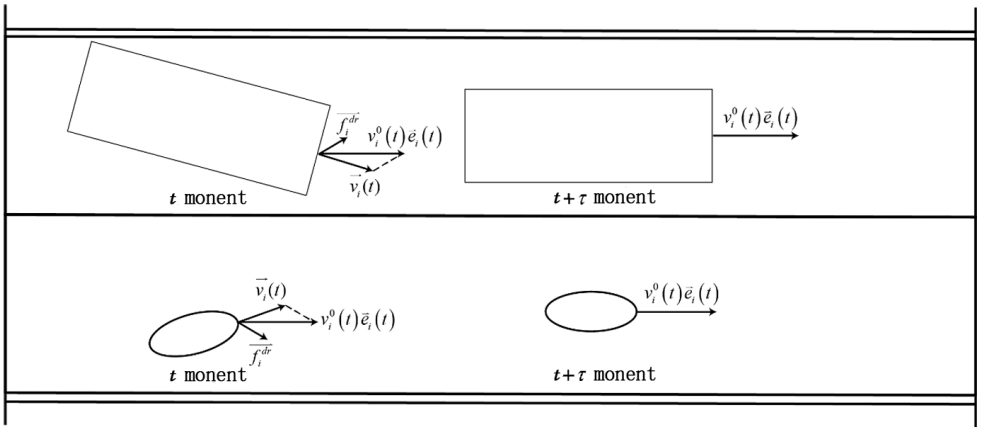

Figure 12 – Schematic diagram of individual units subject to driving forces (The top image represents motorised vehicles and the bottom image represents non-motorised vehicles)

The interaction force between vehicles

To avoid collisions, vehicles maintain a certain safety space, the size of which depends on traffic density, vehicle type and speed. When other vehicles enter the perception field and approach to a certain extent, a repulsive force is generated, which increases as the proximity increases, as shown in *Figure 13*. In this paper, the repulsive force between individuals is derived from the traditional social force model formula [39]. The parameters A_{ji}, r_{ij} are calibrated based on the types of individual units exerting the force. The repulsive force between individuals, denoted as $\vec{f_{ji}^{re}}(t)$, is expressed by *Equation (14):*

$$\vec{f_{ji}^{re}}(t) = exp\left(-\frac{b_{ji}}{r_{ij}}\right)\vec{n}_{ji} \tag{14}$$

In the formula: A_{ji} represents the strength of the repulsive force exerted by individual unit j on individual unit I; r_{ij} denotes the safe perception field action distance in the direction of the line connecting the two vehicles; $\vec{n}_{ji}$ is the directional vector pointing from individual unit j towards individual unit i; b_{ji} signifies the distance between the centre of individual unit i and the outer contour of unit j.

In the context of the model, the expression for the distance b_{ji} from the centre of an individual unit to the outer contour of another vehicle is influenced by the shape of the physical modelling of the individual unit's perception field. When the vehicle exerting the repulsive force ahead is a non-motorised vehicle, the expression for b_{ji} is as shown in *Equation (15).* Conversely, when the vehicle exerting the repulsive force ahead is a motor vehicle, the expression for b_{ji} is presented in *Equation (16).*

$$b_{ji} = d_{ji}\, sec\, \theta_{ji} - \frac{a_j b_j}{2\sqrt{a_j^2\, sin^2\, \theta_{ji} + b_j^2\, cos^2\, \theta_{ji}}} \tag{15}$$

$$b_{ji} = d_{ji}\, sec\, \theta_{ji} - \frac{1}{2} a_j\, sec\, \theta_{ji} \tag{16}$$

In the formula: d_{ji} represents the horizontal distance between the centre points of individual units i and j; a_j, b_j denote the longitudinal and lateral lengths of individual unit j; θ_{ji} is the angle between the actual velocity direction of individual unit I and the line connecting the normal vector of individual unit i with individual unit j.

Individuals experience not only repulsive forces but also attractive forces, as shown in *Figures 13* and *14*. The intensity of these attractive forces depends on the difference in speed, the distance between them, and the distance of the safety perception field. When the distance reaches the safety range, vehicles will maintain a stable following state, as expressed in *Equation (17)*:

$$\begin{cases} \vec{f}_{ij}^{at} = \vec{n}_{ij}\varepsilon_{ij}C_{ij}^2(v_i - v_j) = \vec{n}_{ij}\varepsilon_{ij}\dfrac{(v_i - v_j)^3}{(d_{ji} - r_{ij})^2} \\ C_{ij} = \dfrac{v_i - v_j}{d_{ji} - r_{ij}} \end{cases} \tag{17}$$

In the equation: $\vec{n}_{ij}$ represents the direction vector from the individual unit I to individual unit j; ε_{ij} represents the utility coefficient of the attractive force between individuals; C_{ij} represents the intensity of the following field of the individual unit I towards individual unit j; v_i and v_j represent the speeds of individual units i and j, respectively; d_{ji} represents the horizontal distance between the centres of individual units i and j; r_{ij} represents the safety perception field effective distance in the direction of the line connecting the two vehicles.

A schematic diagram of the individual unit under repulsive force and subject to attraction is shown in *Figures 13* and *14*.

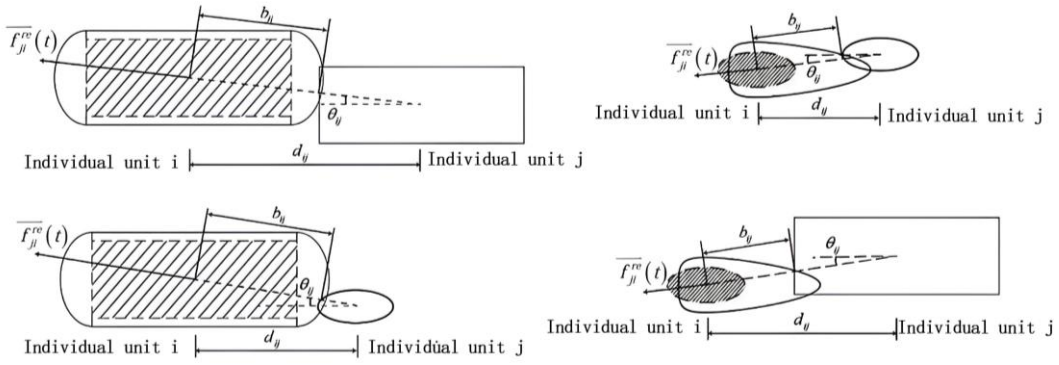

Figure 13 – Schematic representation of repulsive forces on motorised (left) and non-motorised (right) vehicles

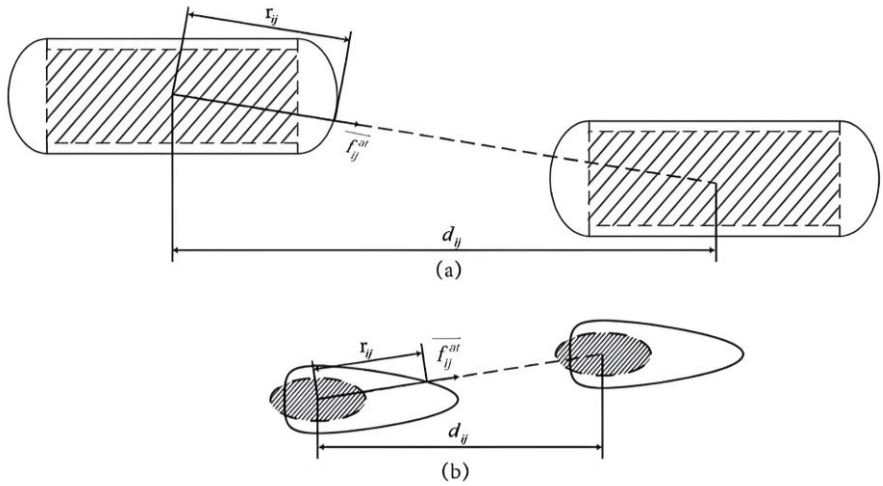

Figure 14 – Motorised (top) and non-motorised (bottom) vehicles subjected to attraction schematics

Boundary forces and lane forces based on artificial potential fields

This paper refers to the artificial potential field and sets up the potential function for obstacles. Based on the road conditions, a road potential field model is established. Road potential functions Ub and Uc are constructed for non-motorised vehicles and motor vehicles, respectively, as shown in *Equations (18)* and *(19)*:

$$U_{b(x,y)} = \begin{cases} \gamma(e^{l_1-y} - l_1 + y - 1) & ,0 \le y \le l_1 \\ \lambda\left\{cos\left[\frac{\pi}{l_2 - l_1}(l_2 - y)\right] + 1\right\} & ,l_1 < y \le l_2 \\ \varphi\left[e^{-(l_2-y)} + l_2 - y - 1\right] + 2\lambda & ,l_2 < y \le l_4 \end{cases} \quad (18)$$

$$U_{c(x,y)} = \begin{cases} \varphi(e^{l_2-y} - l_2 + y - 1) + 2\lambda & ,0 \le y \le l_2 \\ \lambda\left\{cos\left[\frac{\pi}{l_3 - l_2}(y - l_2)\right]\right\} + 1\}, & l_2 < y \le l_3 \\ \gamma[e^{y-l_3} + l_3 - y - 1] & ,l_3 < y \le l_4 \end{cases} \quad (19)$$

Taking the negative gradient of the potential field function yields the boundary force functions corresponding to non-motorised and motor vehicles, as shown in *Equations (20)* and *(21)*:

$$\overrightarrow{f_i^{bb}} = \begin{cases} -\gamma(-e^{l_1-x} + 1) & ,0 \le x \le l_1 \\ -\lambda\left\{sin\left[\frac{\pi}{l_2 - l_1}(l_2 - x)\right] \cdot \frac{\pi}{l_2 - l_1}\right\}, & l_1 < x \le l_2 \\ -\varphi[e^{-(l_2-x)} - 1] & ,l_2 < x \le l_4 \end{cases} \quad (20)$$

$$\overrightarrow{f_i^{bc}} = \begin{cases} -\varphi(-e^{l_2-x} + 1) & ,0 \le x \le l_2 \\ \lambda\left\{sin\left[\frac{\pi}{l_3 - l_2}(x - l_2)\right] \cdot \frac{\pi}{l_3 - l_2}\right\} & ,l_2 < x \le l_3 \\ -\gamma[e^{x-l_3} - 1] & ,l_3 < x \le l_4 \end{cases} \quad (21)$$

In the equations: l_1, l_3 represent the lateral positions of the median lines for non-motorised and motor vehicle lanes, respectively; l_2 is the lateral position of the lane dividing line; l_4 is the horizontal width of the road; γ is the intensity of the boundary guidance effect; λ is the intensity of the lane guidance effect; φ is the intensity of the road borrowing guidance effect.

The study and analysis of the road potential field function in mixed traffic areas of vehicles and non-motorised vehicles are conducted using general environmental and vehicle parameters. The width of the non-motorised vehicle lane, l_2 is set to 3 metres, and the width of the motor vehicle lane, (l_4-l_2), is set to 3.5 metres. The boundary guidance effect intensity, γ, is set to 120 and 200, the lane guidance effect intensity, λ, is set to 80 and 120, and the road borrowing guidance effect intensity, φ, is set to 20 and 40. These values are solely for the study of artificial potential field functions and are not related to physical significance. Based on the set parameters, the potential fields for non-motorised and motor vehicles are established, as shown in *Figures 15* and *16*.

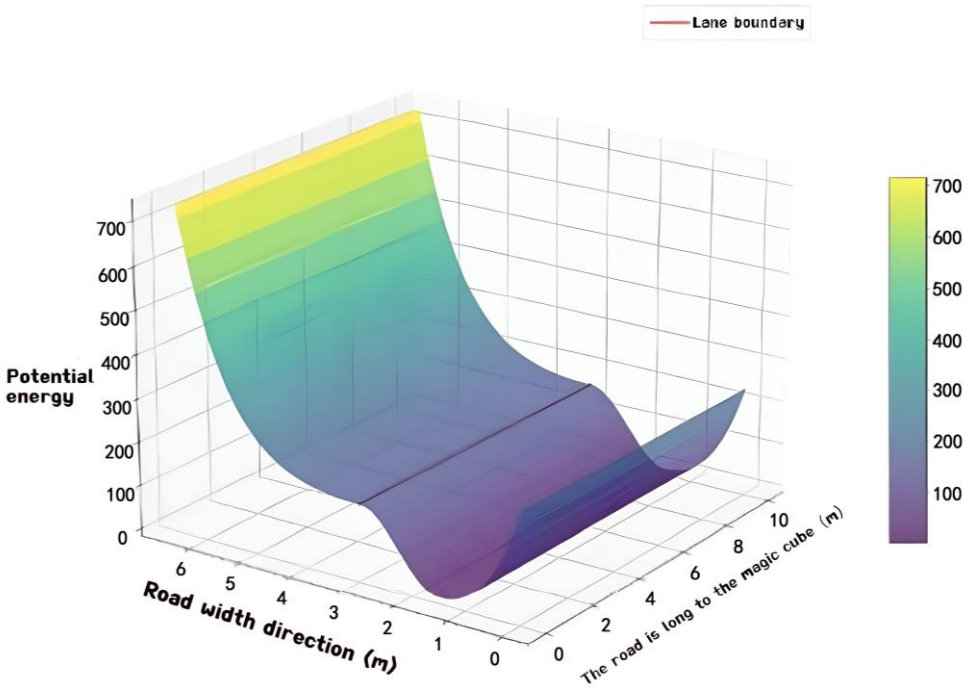

Figure 15 – Non-motorised potential energy field

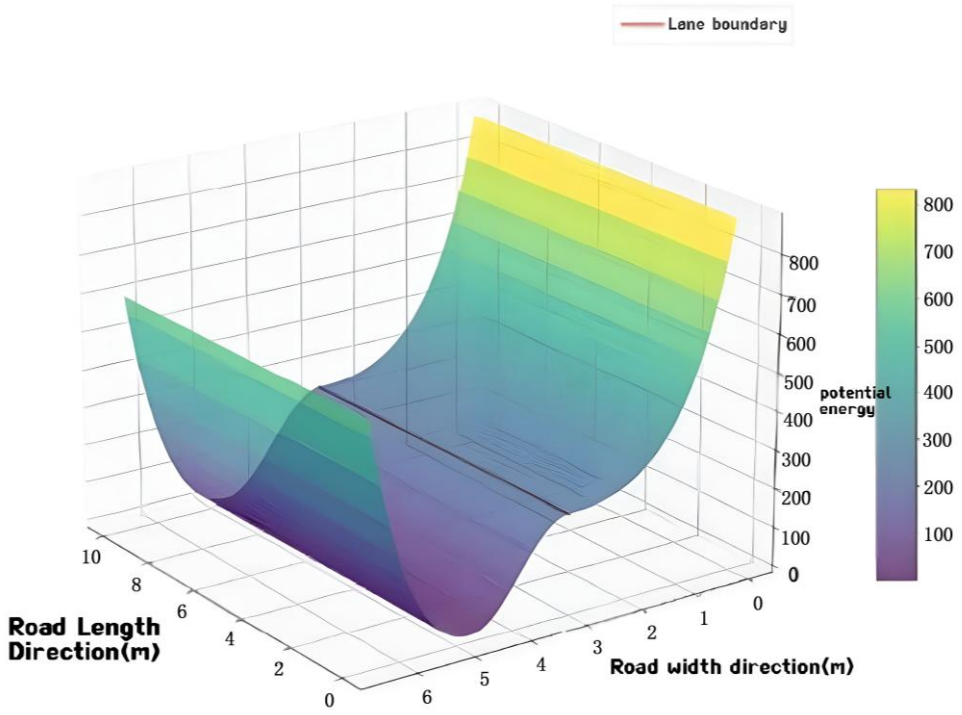

Figure 16 – Motor vehicle potential field

Resultant of forces

Based on the aforementioned analysis of the forces acting on vehicles in mixed traffic sections, including driving force, inter-individual forces and boundary forces, an improved social force model based on artificial potential fields is established. In this model, the resultant force acting on individual units is reflected in their operational state. The specific resultant forces for non-motorised and motor vehicles are shown in *Equation (22)*:

$$\begin{cases} \overrightarrow{F_b} = \vec{f_i^{dr}} + \vec{f_{ij}^{re}} + \vec{f_{ij}^{at}} + \vec{f_i^{bb}} \\ \overrightarrow{F_c} = \vec{f_i^{dr}} + \vec{f_{ij}^{re}} + \vec{f_{ij}^{at}} + \vec{f_i^{bc}} \end{cases} \tag{22}$$

In the equation: $\vec{f_i^{dr}}$ represents the driving force of the vehicle; $\vec{f_{ij}^{re}}$ represents the repulsive force between motor vehicle individual units; $\vec{f_{ij}^{at}}$ represents the attractive force between individual units; $\vec{f_i^{bb}}$ represents the boundary force experienced by non-motorised vehicles; $\vec{f_i^{bc}}$ represents the boundary force experienced by motor vehicles.

4. IMPROVEMENT OF THE SOCIAL FORCE MODEL PARAMETER CALIBRATION

The parameter calibration component of the enhanced social force model is predicated on the team's empirically measured data and predefined parameters. The model is distinguished by its attribution of real-world significance to each parameter, thereby enhancing its applicability.

4.1 Calibration of physical attributes of motor vehicles and non-motor vehicles and parameters for mixed flow scenarios

1) The non-motorised individual unit model is elliptical, with the cyclist's pedal centre as the centre of the circle, a longitudinal axis length of 1.8 metres, a transverse axis length of 0.8 metres, and a total mass of 120 kilograms, including an average mass of 65 kilograms for the cyclist and 55 kilograms for the electric bike. The schematic diagram of motor vehicles and non-motorised vehicles is shown in *Figures 17* and *18.*
2) This section includes two parameters: the width of the motor vehicle lane L_{lane}^{car} and the width of the non-motorised vehicle lane L_{lane}^{bike}, both of which are data measured and calibrated on-site. The width of the motor vehicle lane L_{lane}^{car} is 3.5 metres, and the width of the non-motorised vehicle lane L_{lane}^{bike} is 3.5 m.

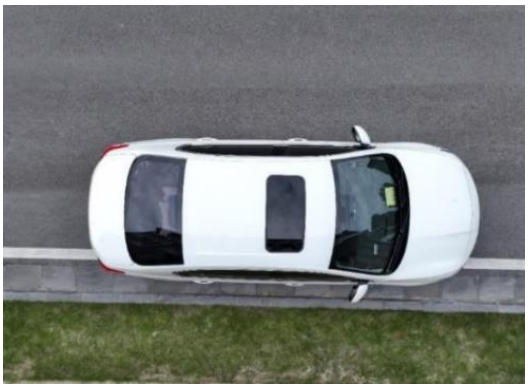

Figure 17 – Schematic diagram of a motor vehicle

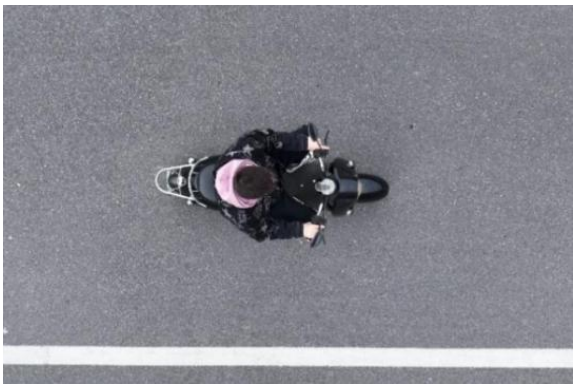

Figure 18 – Schematic diagram of non-motorised vehicles

4.2 Calibration of vehicle perception model parameters

The primary objective of this study is to examine the relationship between the interaction forces of motorised and non-motorised vehicles. The establishment of the perception domains of motorised and non-motorised vehicles is imperative for the enhancement of the social force model.

Calibration of parameters related to the perception domain of non-motorised vehicles

This paper introduces a compression effect value β to describe the variation of the perceived space in the non-motorised traffic perception model with changes in traffic density. According to *Equation (4)*, the perceived space decreases as the traffic density increases. In actual traffic surveys, the jam density k_j value of 0.8 was selected for calibrating the current traffic density in simulations.

The longitudinal reaction coefficient α_i^h is related to the longitudinal reaction time. According to reference [52], its value is taken as 0.8 seconds. The anisotropy coefficient λ_i^s reflects the influence of individuals in different directions on the ego vehicle. A value of 1 indicates that the influence is the same in all directions, a value less than 1 indicates that the forward influence is greater than the rear influence, and a value of 0 means that the rear influence is ignored. Based on reference [53], the anisotropy coefficient λ_i^s in this paper is selected to be 0.7, and the adjustment coefficient s_λ is 4.

Calibration of parameters related to the perception domain of motor vehicles

The parameters that need to be calibrated for the motor vehicle perception domain constructed in this paper include the longitudinal perception distance $d_i^{hc}$and the lateral perception distance d_i^{vc} for motor vehicles. Based on actual survey data, the longitudinal perception distance d_i^{hc} is determined to be 1 metre, and the calculation for the lateral perception distance is described in the following text.

4.3 Calibration of vehicle motion model series parameters

The primary focus of vehicle motion model parameter calibration is on force analysis and conventional parameters such as acceleration and deceleration times. The refinement of the perception domain of motor vehicles is enhanced by detailed calibration, thereby increasing its applicability.

Calibration of driving force parameters

1) Expected speed of the vehicle $v_i^0(t)$

This section of the road is mixed traffic for both vehicles and non-motorised transport, and according to the survey data, the desired speed of motor vehicles is 17.29 km/h. The distribution of individual unit velocities is shown in *Figures 19* and *20.*

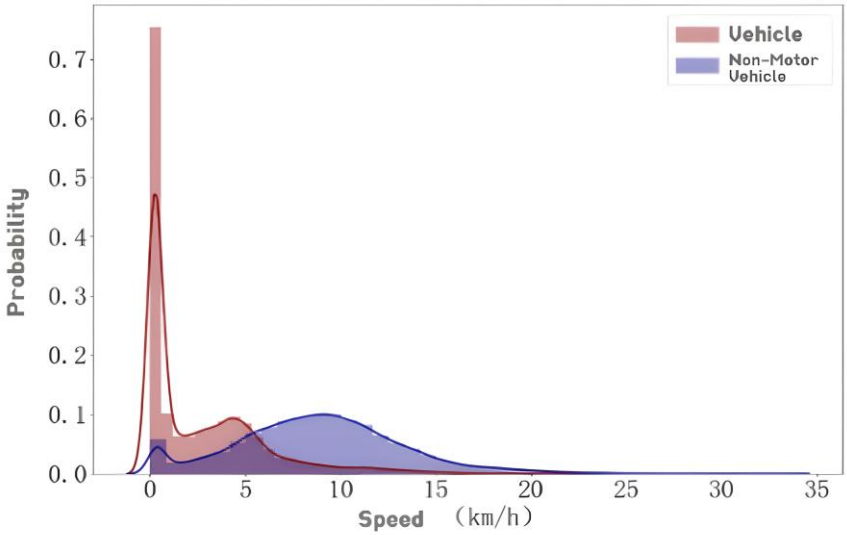

Figure 19 – Probability distribution of individual cell speeds during peak periods

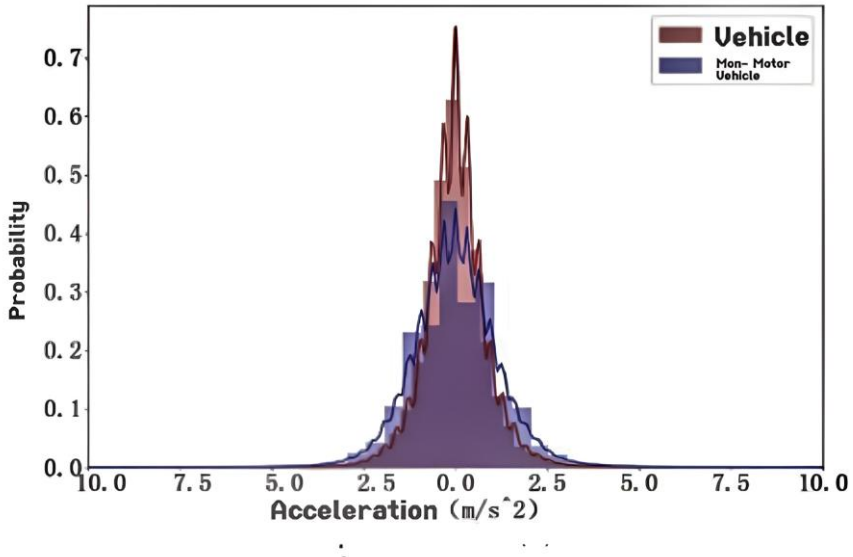

Figure 20 – Probability distribution of individual cell acceleration at peak

2) Duration τ_i

The duration refers to the time it takes for a vehicle to accelerate from its current speed to the desired speed, including the driver's reaction time and the time for acceleration manoeuvres. The calculation is as follows:

$$\tau_i = t_{reaction} + t_{control} \tag{23}$$

In the equation, according to relevant studies, the driver's reaction time is taken as 1 second, and the control time is calculated based on the following formula:

$$t_{control} = \frac{v_e - v}{a} \tag{24}$$

In the equation: v_e represents the desired speed; v represents the average speed; a represents the acceleration.

Substituting the values, we get the control time for non-motorised vehicles as 0.25 seconds, and the control time for motor vehicles as 1 second.

Calibration of interaction force parameters

1) Repulsion force parameters:

The repulsion force intensity is A_{ij}, the repulsion force utility coefficient μ_{ij}, and the lateral safety distances d^{vb}, d^{vc}. Two individual units driving side by side are selected to calibrate the repulsion force intensity A_{ij} and the repulsion force utility coefficient μ_{ij} as shown in *Figure 21.*

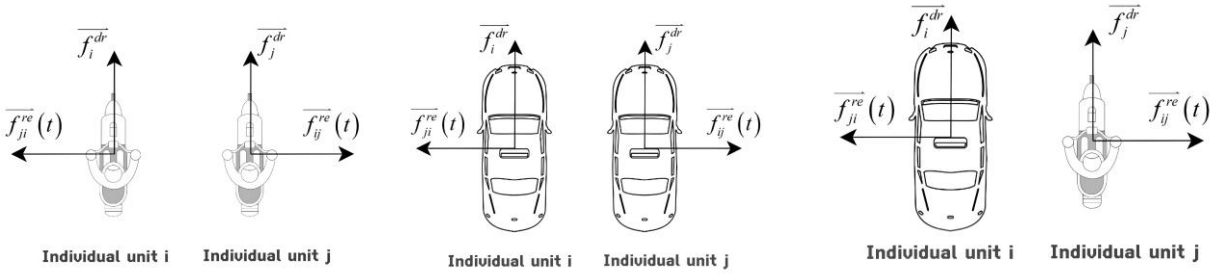

Figure 21 – Schematic of repulsive forces on different individual units travelling side by side

At this point, the individual unit is only subject to the driving force and the repulsive force, and the lateral component of acceleration is entirely contributed by the driving force, while the longitudinal component is entirely contributed by the repulsive force. According to the social force model, the calculated longitudinal acceleration of individual unit i is as follows:

$$\hat{a}_{ij}^{re}(t) = \frac{f_{ij}^{re}}{m_i} = \frac{A_{ij}\mu_{ij}\, exp\left(-\frac{b_{ij}}{r_{ij}}\right)}{m_i} \tag{25}$$

When two individual units are driving side by side, r_{ij} in the above formula represents the lateral radius of the vehicle's perception domain. In mixed traffic sections with both vehicles and non-motorised transport, the sources of repulsive forces include both motor vehicles and non-motorised vehicles. For each specific type of vehicle, the product of A_{ij} and μ_{ij} is uniquely determined. Therefore, in the following narrative of the calculation formula, $A_{ij}\mu_{ij}$ is considered as a single parameter. Let the measured value of the longitudinal acceleration of individual unit i be $a_{ij}^{re}(t) = a_{y,i}(t)$ and taking the logarithm of both sides of the above formula yields the sum of the squared residuals of the longitudinal acceleration as follows:

$$\begin{aligned} E\& &= \sum_{i=1}^{n} \left(ln\left(a_{y,i}(t)\right) - ln\left(\hat{a}_{ij}^{re}(t)\right)\right)^2 \\ &= \sum_{i=1}^{n} \left(ln\left(a_{y,i}(t)\right) - ln\left(\hat{A}_{ij}\hat{\mu}_{ij}\right) + ln(m_i) + b_{ij}/\hat{r}_{ij}\right)^2 \end{aligned} \tag{26}$$

According to the method of least squares, we take the partial derivatives of *Equation (24)* with respect to $\ln\left(\hat{A}_{ij}\hat{\mu}_{ij}\right)$ and $\hat{r}_{ij}^{-1}$, set them to zero, and solve the system of equations to obtain:

$$\hat{A}_{ij}\hat{\mu}_{ij} = m_i\, exp\left(\frac{1}{n}\sum_{i=1}^{n} ln\left(a_{y,i}(t)\right) + \frac{1}{n\hat{r}_{ij}}\sum_{i=1}^{n} b_{ij}\right) \tag{27}$$

$$\hat{r}_{ij} = \frac{\left[\left(\sum_{i=1}^{n} b_{ij}\right)^2 - n\sum_{i=1}^{n} b_{ij}^2\right]}{\left[n\sum_{i=1}^{n} b_{ij}\, ln\left(a_{y,i}(t)\right) - \sum_{i=1}^{n} ln\left(a_{y,i}(t)\right)\sum_{i=1}^{n} b_{ij}\right]} \tag{28}$$

Based on the actual measured data of free flow during off-peak hours on a certain cross-river bridge, the repulsion force utility coefficient for non-motorised vehicles is set to 1, and the repulsion force action intensity for individual units is 202 N. The repulsion force utility coefficient for motor vehicles is 1.67. The optimal estimated values for the lateral radius of the perception domain for vehicles and non-motorised vehicles are 1.24 m and 0.63 m, respectively, with corresponding lateral safety distances of 0.34 m and 0.23 m. The calibration results for repulsion force-related parameters are shown in *Table 1:*

Table 1 – Calibration of repulsive force parameters

Target car	$A_{ij}\mu_{ij}/\mathbb{N}$	μ_{ij}	Current car	$\hat{r}_{ii} = 1/2b_i + d_v$
Motor vehicle	313	1.67	Motor vehicle	1.24
Non-motorised vehicle	202	1.00	Non-motorised vehicle	0.63

2) Attractiveness utility coefficient ε_{ij}:

$$\hat{a}_i(t) = \frac{\left(f_i^{dr} + f_{ij}^{at}\right)}{m_i} = \hat{a}_i^{dr} + \varepsilon_{ij}\frac{\left(v_i - v_j\right)^3}{m_i\left(d_{ij} - r_{ij}\right)^2} \tag{29}$$

Based on the actual measured data of free flow during off-peak hours on a certain cross-river bridge within the surveyed area, the above formula is used for fitting, and the estimated values of the attractive force utility coefficient ε_{ij} are obtained as shown in *Table 2.*

Table 2 – Calibration of attraction effect coefficient

Front and rear car combination	Attractiveness utility coefficient ε_{ij}
Motor vehicles - Motor vehicles	15
Motor vehicles - Nonmotor vehicles	20
Non-motorised vehicles - Motor vehicles	10
Non-motorised vehicles - Non-motorised vehicles	20

Boundary force parameter calibration

According to the measured data of the auxiliary road near the intersection in a certain section of the surveyed area, the calibration results of the parameters are shown in *Figure 22, Figure 23* and *Table 3:*

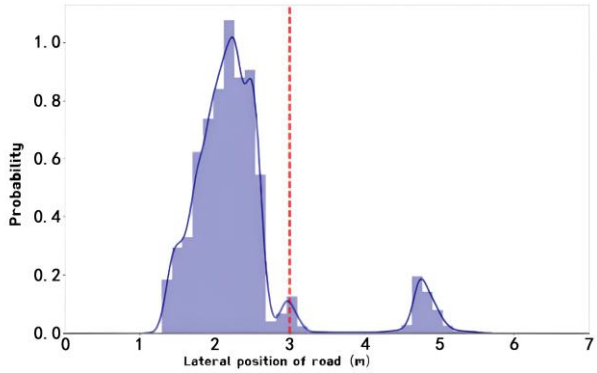

Figure 22 – Roadway lateral motor vehicle density distribution (by vehicle and lane line distance)

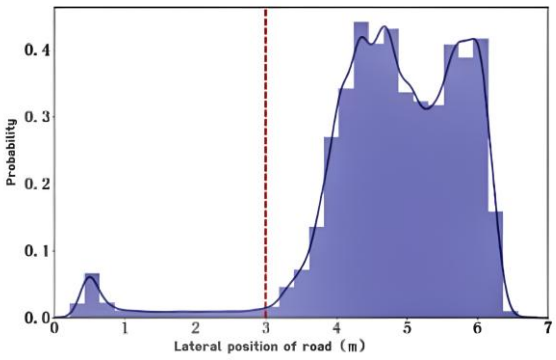

Figure 23 – Roadway lateral non-motorised density distribution (by vehicle and lane line distance)

Table 3 – Calibration of guidance strength parameters

Parameter	Effect on motor vehicles	Effect on non-motorised vehicles
Strength of boundary guidance effect γ	30	10
Strength of lane guidance function λ	7	2
Strength of the borrowed lane guidance effect φ	5	1.5

5. SIMULATION VALIDATION OF IMPROVED SOCIAL FORCE MODEL

The simulation verification component of the enhanced social force model employs the calibrated parameter data from the preceding text to simulate the social forces between motorised and non-motorised vehicles and validate them based on measured data.

5.1 Simulation platform construction

To verify the correctness and effectiveness of the proposed model, this paper uses Python to build the platform from five modules: the main function, A* algorithm, social force simulation model, vehicles and visualisation.

1) The main function module is responsible for invoking the vehicle module and the visualisation module, creating a list of vehicles, initialising each vehicle, and thus controlling the operation of the simulation platform.
2) The A* algorithm module is primarily used to achieve macro path control for non-motorised vehicles to avoid obstacles and navigate to destination points.
3) The vehicle module is an important functional part for controlling the movement of individual units.
4) The social force simulation model module is the core part for implementing the micro-motion of vehicles, compiled using the Python language, including the construction of the perception field and the mechanical model:

Perception field: Divided into the non-motorised vehicle perception field and the motor vehicle perception field. Non-motorised vehicle perception field calculation: refers to the actual speed direction of the non-motorised vehicle and returns the front distance of the non-motorised vehicle perception field in a given two-vehicle connection direction. Motor vehicle perception field calculation: returns the longitudinal and lateral dimensions of the motor vehicle perception field.

Mechanical model: Includes self-driving force, inter-individual interaction forces (repulsive and attractive forces), boundary forces based on artificial potential fields and the calculation of the resultant force.

The basic simulation process diagram is shown in *Figure 24*.

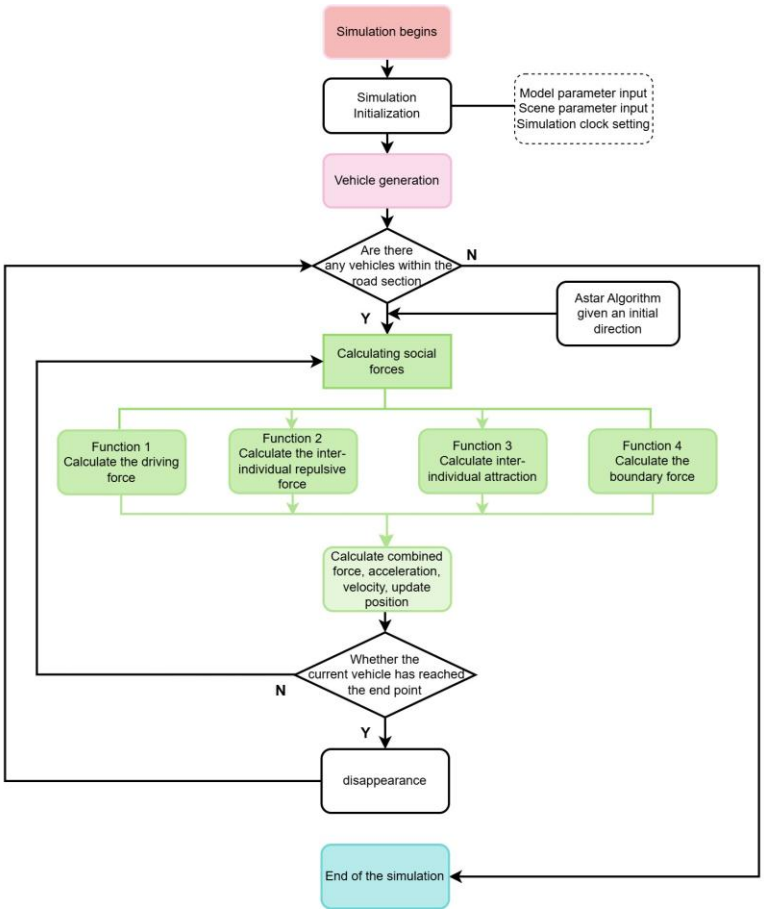

Figure 24 – Basic simulation process diagram

5.2 Basic diagram verification

Taking the southwest side auxiliary road of Machicun intersection on Minzu Avenue as an example, the actual scene data includes: the width of the motor vehicle lane is 3.5 metres, the width of the non-motorised vehicle lane is 3 metres, the proportion of non-motorised vehicles is 73.8%, and the proportion of motor vehicles is 26.2%. The simulation area is set to be 150 metres long, and three repeated experiments are conducted. The simulation data are compared with the actual survey data. A total of 1,068 data points were obtained from the simulation, showing that the maximum density of mixed traffic is approximately 0.34 bikes/m², the maximum speed of non-motorised vehicles is 26.98 km/h, the maximum speed of motor vehicles is 18.11 km/h, and the overall average speed is 23.29 km/h. An independent sample T-test with a 95% confidence level indicates that the significance of variance and mean are 0.68 and 0.40, respectively, both of which are greater than 0.05, suggesting that there is no significant difference between the two sets of data, just as shown in *Table 4.*

Table 4 – Independent sample test for survey and simulation data

	Levine's test of variance equivalence			**Mean equivalence test**	
	F	Significance level	t	Degree of freedom	Significance (two-tailed)
The equal variance assumption	0.170415	0.679951	0.833747	426	0.404891
Heteroskedasticity assumption			0.819135	426	0.335742

The summary statistics of the survey and simulation data are shown in *Figure 25* and *Table 5,* and it can be seen that there is a strong linear relationship between density-velocity obtained from both survey and simulation data.

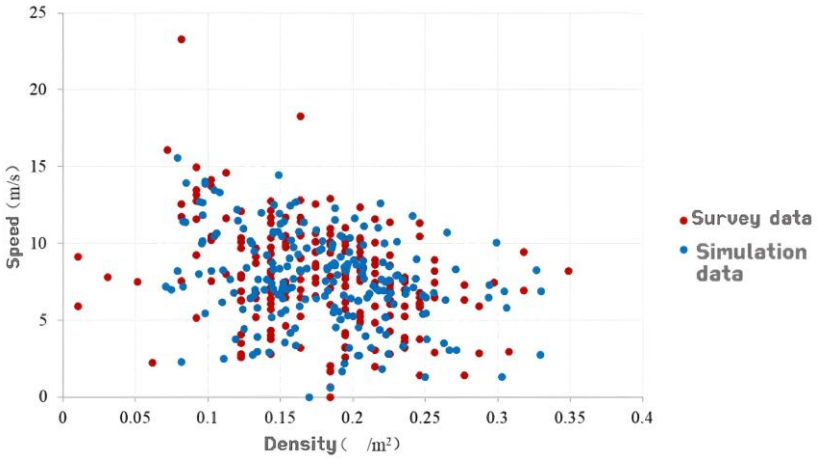

Figure 25 – Survey and simulation density velocity plot

Table 5 – Comparison of survey and simulation data

Positioning		**Free speed km/h**			**Jam density bike/m²**	
	survey	simulation	error value	survey	simulation	error value
Minzu Avenue, Makura Intersection	20.87	22.53	0.07954	0.502	0.535	0.065737
The auxiliary road of University Avenue East	31.15	29.77	-0.0443	0.463	0.427	-0.07775
Northern Bridge	36.03	34.68	-0.03747	0.481	0.472	-0.01871
Zhongxing Bridge	32.62	29.71	-0.08921	0.494	0.51	0.032389

From the above, it can be seen that the survey and simulation data errors are within a reasonable range, indicating that the model constructed in this paper has good applicability for simulating mixed driving scenarios of motor vehicles and nonmotor vehicles.

6. CONCLUSION

This study validated the effectiveness of the micro-mixed traffic flow model through simulation and density-speed diagrams, demonstrating the model's accuracy in simulating the actual behaviour of motorised and non-motorised vehicles. Addressing the shortcomings of the social force model in describing non-motorised vehicle behaviour, this study introduced artificial potential fields to improve boundary forces and lane forces, replacing traditional boundary forces with continuous lateral potential fields, considering the guidance and isolation effects of road dividers and curbs, and enhancing the model's ability to describe the impact of traffic boundaries and active overtaking behaviour. The study optimised the design of the non-motorised vehicle's perception field, proposed a shield-shaped perception field model to reflect the perception capabilities of cyclists more realistically, and introduced anisotropic coefficients and dynamic compression coefficients to accurately simulate the dynamic changes in the perception field in actual traffic, providing a new perspective for the simulation of mixed traffic flows.

REFERENCES

[1] Song Z, et al. Quantitative analysis of impact of bicycle on the vehicle speed in urban mixed traffic. *Journal of* Railway *Science and Technology*. 2017;14(8):1783-1791. DOI: 10.19713/j.cnki.43-1423/u.2017.08.027.

[2] Lin G, et al. Impact of bicycle traffic on vehicle operation on divided road. *Journal of Highway and* Transportation *Research and Development.* 2016;33(1):112-118. DOI: 10.3969/j.issn.1002-0268.2016.01.017.

[3] Feng X, et al. Simulation of mixed traffic flow by cellular automaton considering bicycle flow characteristics. Journal *of Highway and Transportation Research and Development*. 2016;33(3):132-137. DOI: 10.3969/j.issn.1002-0268.2016.03.022.

[4] Qin L, et al. Capacity and LOS of urban arterial road segment under the interference of bicycle. *Journal of Harbin Institute of Technology.* 2018;50(9):61-67. DOI: 10.11918/j.issn.0367-6234.201708016.

[5] Schaefer JS, et al. Empirical study of the impacts of bicycles on passenger car speeds on urban roads without bicycle lanes. *Transportation Research Record: Journal of the Transportation Research Board*. 2021;2675(9):664-674. DOI: 10.1177/03611981211004122.

[6] Apasnore P, et al. Bicycle-vehicle interactions at mid-sections of mixed traffic streets: Examining passing distance and bicycle comfort perception. *Accident Analysis & Prevention*. 2017;106:141-148. DOI: 10.1016/j.aap.2017.05.003.

[7] Dailisan DN, et al. Agent-based modeling of lane discipline in heterogeneous traffic. *Physica A: Statistical Mechanics and its* Applications*.* 2016;457:138-147. DOI: 10.1016/j.physa.2016.03.104.

[8] Shao H , et al. Electric bicycle lane-changing behavior under strategy games. *Sustainability*. 2018;10(9):3019. DOI: 10.3390/su10093019.

[9] Liu Y, et al. Modeling lateral interactions between motorized vehicles and non-motorized vehicles in mixed traffic using accelerated failure duration model. *Transportmetrica A: Transport Science*. 2022;18(3):910-933. DOI: 10.1080/23249935.2021.1908443.

[10] Petzoldt T, et al. Drivers' gap acceptance in front of approaching bicycles – Effects of bicycle speed and bicycle type. *Safety Science*. 2017;92:283-289. DOI: 10.1016/j.ssci.2015.07.021.

[11] Tang TQ, et al. A dynamic model for the heterogeneous traffic flow consisting of car, bicycle, and pedestrian. *International Journal of* Modern *Physics C*. 2010;21(02):159-176. DOI: 10.1142/s0129183110015038.

[12] Mathew TV, et al. Strip-Based approach for the simulation of mixed traffic conditions. *Journal of Computing in Civil Engineering*. 2015;29(5):04014069. DOI: 10.1061/(asce)cp.1943-5487.0000378.

[13] Papathanasopoulou V, et al. Flexible car–following models for mixed traffic and weak lane–discipline conditions. *European Transport* Research *Review*. 2018;10(2):62. DOI: 10.1186/s12544-018-0338-0.

[14] Meng J , et al. Cellular automaton model for mixed traffic flow with motorcycles. *Physica A: Statistical Mechanics and its Applications.* 2007;380:470-480. DOI: 10.1016/j.physa.2007.02.091.

[15] Jia N, et al. Meta-cellular automata modeling of motor vehicle traffic flow under bicycle interference. *Systems Engineering - Theory & Practice*. 2010;30(7):1333-1339. DOI: 10.12011/1000-6788(2010)7-1333.

[16] Luo Y, et al. Modeling the interactions between cars and bicycles in heterogeneous traffic. *Journal of Advanced Transportation*. 2015;49(1):29-47. DOI: 10.1002/atr.1257.

[17] Helbing D, et al. Social force model for pedestrian dynamics. *Physical Review E*. 1995;51(5):4282-4286. DOI: 10.1103/physreve.51.4282.

[18] Zhang R, et al. An improved social force model considering the shift and deceleration of the overtaken non-motorized vehicle. *Science Technology and Engineering*. 2022;22(34):15367-15371. DOI: 10.3969/j.issn.1671-1815.2022.34.046.

[19] Rui YX, et al. An improved social force model for bicycle flow in groups. *Journal of Advanced Transportation*. 2021;2021:1-14. DOI: 10.1155/2021/2412655.

[20] Qin J, et al. Modeling and simulation for non-motorized vehicle flow on road based on modified social force model. *Mathematics*. 2022;11(1):170. DOI: 10.3390/math11010170.

[21] Dong H. *Simulation research on two-way bicycle traffic flow based on social force model*. Master's thesis. Chang'an University; 2021.

[22] Wang Z. *Simulation research on social force model of non-motorized vehicles turning left at intersection*. Master's thesis. Beijing Architecture University; 2023.

[23] Wang W, et al. Modeling of electric bicycle behavior in unidirectional flow based on improved social forces. *Journal of Transportation Systems Engineering and Information Technology*. 2022;22(5):223-232. DOI: 10.16097/j.cnki.1009-6744.2022.05.023.

[24] Yang D, et al. Modeling and simulation of motor vehicle-electric bicycle traffic flow at signalized intersection. *Journal of Harbin Institute of Technology*. 2018;50(8):181-187. DOI: 10.11918/j.issn.0367-6234.201705120.

[25] Qu Z , et al. Modeling electric bike–car mixed flow via social force model. *Advances in Mechanical Engineering*. 2017;9(9):168781401771964. DOI: 10.1177/1687814017719641.

[26] Jensen E, et al. Using artificial potential fields to model driver situational awareness. *IFAC-PapersOnLine*. 2022; 55(41):148-153. DOI: 10.1016/j.ifacol.2023.01.118.

[27] Xu Y, et al. Simulation of turning vehicles' behaviors at mixed-flow intersections based on potential field theory. *Transportmetrica B: Transport Dynamics*. 2019;7(1):498-518. DOI: 10.1080/21680566.2018.1447407.

[28] Xie S, et al. Distributed motion planning for safe autonomous vehicle overtaking via artificial potential field. *IEEE Transactions on Intelligent Transportation Systems*. 2022;23(11):21531-21547. DOI: 10.1109/tits.2022.3189741.

[29] Zhang J, et al. Path planning and tracking control for vehicle overtaking on curve based on modified artificial potential field method. *Automotive Engineering*. 2021;43(4):546-552. DOI: 10.19562/j.chinasae.qcgc.2021.04.012.

[30] Qiu P, et al. Unmanned vehicle path planning based on structured road improved artificial potential field method. *Machinery Design & Manufacture*. 2023;(03):291-296. DOI: 10.19356/j.cnki.1001-3997.2023.03.011.

[31] Tang Z, et al. Vehicles path planning and tracking based on an improved artificial potential field method. *Journal of Southwest University (Natural Science)*. 2018;40(6):174-182. DOI: 10.13718/j.cnki.xdzk.2018.06.025.

[32] Wang X, et al. Research on autonomous vehicle local path planning method based on improved artificial potential field algorithm. *Computer & Digital Engineering*. 2022;50(3):554-558+630. DOI: 10.3969/j.issn.1672-9722.2022.03.019.

[33] Guo M, et al. Unmanned vehicle path planning and tracking control based on improved artificial potential field method. *Journal of System Simulation*. 2024;36(10):2423-2434. DOI: 10.16182/j.issn1004731x.joss.23-0768.

[34] Ji P, et al. Local path planning for unmanned ground vehicles based on improved artificial potential field method in frenet coordinate system. *Acta Armamentarii*. 2024;45(07):2097-2109. DOI: 10.12382/bgxb.2023.0305.

[35] Wang P, et al. Obstacle avoidance path planning design for autonomous driving vehicles based on an improved artificial potential field algorithm. *Energies*. 2019;12(12): 2342. DOI: 10.3390/en12122342.

[36] Kong H, et al. Path planning for intelligent vehicle collision avoidance based on improved artificial potential field method. *Journal of Hefei University of Technology (Natural Science)*. 2023;46(5): 583-589. DOI: 10.3969/j.issn.1003-5060.2023.05.002.

[37] Wang Q, et al. Lane keeping coordination control based on parameter-varying artificial potential field. *Chinese Journal of Mechanical Engineering*. 2018;54(18):105-114. DOI: 10.3901/JME.2018.18.105.

[38] Li S, et al. Active obstacle avoidance path planning based on improved artificial potential field method in front vehicle cut-in scenario. *Journal of Jiangsu University(Natural Science Edition)*. 2023;44(1):7-13. DOI: 10.3969/j.issn.1671-7775.2023.01.002.

[39] Hu H, et al. An improved artificial potential field model considering vehicle velocity for autonomous driving. *IFAC-PapersOnLine*. 2018;51(31):863-867. DOI: 10.1016/j.ifacol.2018.10.095.

[40] Zhou D, et al. Mining the micro-trajectory of two-wheeled non-motorized vehicles based on the improved YOLOx. *Sensors*. 2024;24(3):759. DOI: 10.3390/s24030759.

[41] Ge Z, et al. YOLOX: Exceeding YOLO Series in 2021. *arXiv e-prints*. 2021. DOI: 10.48550/arXiv.2107.08430.

[42] Wojke N, et al. Simple online and realtime tracking with a deep association metric.*2017 IEEE International Conference on Image Processing (ICIP), 2017, 17-20 Sep.2017. Beijing, China.* 2017;3645-3649. DOI: 10.1109/icip.2017.8296962.

[43] Bewley A, et al. Simple online and realtime tracking. 2016 IEEE International Conference on Image Processing (ICIP),2016,25-28 Sep.2016, Phoenix Convention Center, Phoenix, Arizona, USA. 2016;3464-3468. DOI: 10.1109/ICIP.2016.7533003.

[44] Tao S. *Binary mixed traffic characteristics based on bicycle and electric bicycle*. Master's thesis. Chang'an University; 2015.

[45] Li S, et al. Driving characteristics and speed behaviour parameters of direct traffic at intersections based on field driving tests. *Promet - Traffic&Transportation*. 2024;36(6):1022–1038. DOI: 10.7307/ptt.v36i6.587.

[46] Xu H, et al. What road elements are more important than others for safe driving on urban roads? *Promet - Traffic&Transportation*. 2023;*35*(6):814–828. DOI: 10.7307/ptt.v35i6.394.

[47] Li Y, et al. A social force avoidance model and simulation considering micro differences of pedestrians. *Transportation Standardization.* 2023;9(2):33-41. DOI: 10.16503/j.cnki.2095-9931.2023.02.004.

[48] Yan Q. *Research on mixed non-motorized flow simulation based on social force model*. Master's thesis. Beijing Architecture University; 2020.

[49] Yang M. *Micro simulation study of non motorized vehicles considering retrograde effects*. Master's thesis. Beijing Architecture University; 2023.

[50] Tan T. *Research on intrusion effect of straight e-bike at irregular signalized intersection*. Master's thesis. Nanjing: Nanjing Forestry University; 2023.

[51] Jin S, et al. Lane width-based cellular automata model for mixed bicycle traffic flow. *Computer-Aided Civil and Infrastructure Engineering*. 2019;34(8):696-712. DOI: 10.1111/mice.12445.

[52] Liang X. *Dynamic model to simulate bicycle microscopic behavior*. Master's thesis. Beijing Jiaotong University, 2012.

[53] Ye S. *Research on slow traffic simulation based on netlogo and social force model*. Master's thesis. Shenzhen University, 2021.